
Article:
Zhu, X, Zhang, Z, Yang, K et al. (8 more authors) (2018) Characterisation of pore structure development of alkali-activated slag cement during early hydration using electrical responses. Cement and Concrete Composites, 89. pp. 139-149. ISSN 0958-9465

https://doi.org/10.1016/j.cemconcomp.2018.02.016

Characterisation of pore structure development of alkali-activated slag cement during early hydration using electrical responses

Xiaohong ZHU[a], Zhilu ZHANG[a], **Kai YANG[a,b*]**, Bryan Magee[c], Yaocheng WANG[d], **Linwen YU[a*]**, Sreejith NANUKUTTAN[e], Qing LI[a], Song Mu[f], Changhui YANG[a], and Muhammed Basheer[b]

a: College of Materials Science and Engineering, Chongqing University, Chongqing, China
b: School of Civil Engineering, University of Leeds, Leeds, UK
c: Built Environment Research Institute, Ulster University, UK
d: School of Civil Engineering, Shenzhen University, Shenzhen, China
e: School of Natural and Built Environment, Queen's University Belfast, Belfast, UK
f: Jiangsu Provincial Institute of Building Science, Nanjing, China

Abstract

This paper describes the results of a study investigating early age changes in pore structure of alkali-activated slag cement (AASC)-based paste. Capillary porosity, pore solution electrical conductivity and electrical resistivity of hardened paste samples were examined and the tortuosity determined using Archie's law. X-ray computed micro-tomography (X-ray μCT) and Scanning electron microscope (SEM) analysis were also carried out to explain conclusions based on electrical resistivity measurements. AASC pastes with 0.35 and 0.50 water-binder ratios (w/b) were tested at 3, 7, 14 and 28 days and benchmarked against Portland cement (PC) controls. Results indicated that for a given w/b, the electrical resistivity and capillary porosity of the AASC paste were lower than that of the PC control, whilst an opposite trend was observed for the pore solution conductivity, which is due to AASC paste's significantly higher ionic concentration.

Further, capillary pores in AASC paste were found to be less tortuous than that in the PC control according to estimations using Archie's law and from the results of X-ray μCT and SEM analysis. In order to achieve comparable levels of tortuosity, therefore, AASC-based materials are likely to require longer periods of curing. The work confirms that the electrical resistivity measurement offers an effective way to investigate pore structure changes in AASC-based materials, despite threshold values differing significantly from PC controls due to intrinsic differences in pore solution composition and microstructure.

Keywords

Pore tortuosity, alkali-activated slag cement, pore solution, electrical resistivity, capillary porosity, X-ray μCT

1. Introduction

According to the Intergovernmental Panel on Climate Change (IPCC) [1], emissions of greenhouse gases such as CO_2 have increased dramatically over past few decades due to human activities. It is predicated that the possibility of triggering the 2°C danger-limit will rise to 75% if the emission of CO_2 rises beyond 50 Gt by 2020 [2-3]. Due to decomposition of limestone and consumption of fuels during the manufacture, the conventional Portland cement (PC) industry was responsible for 5-8% of the total manmade CO_2 in 2014 [2, 4]. This situation is driving numerous researchers to develop competing low-CO_2 binders, including calcium sulphoaluminate, magnesium and alkali-activated based binders [2, 5].

Alkali-activated slag cement (AASC) is a clinker-free binder comprising ground granulated blast furnace slag (GGBFS) sourced from metallurgical industries. It is estimated that the production of one tonne of AASC generates approximately 0.18 tonnes CO_2; a value significantly lower than for conventional PC [4-6]. Furthermore, AASC, which could be considered as an organic supplement to the conventional PC system, offers a range of high performance characteristics not easily achieved by PC, including excellent mechanical strength, resistance to acid and sulphate attack, and capability for immobilising heavy metals [5-7]. As AASC-based materials are not fully covered in other British Standards for cement and concrete, the British Standards Institution has recently published PAS: 8820 (2016) [8] to encourage their use in the construction industry. It is established that chemical reaction kinetics and hydration products differ significantly between AASC and PC [2, 5], calling into question the suitability of using established PC-based material quality assessment methods for testing AASC-based products. One of the primary issues requiring clarification is about the minimum duration of curing required for the AASC systems in order to result in comparable pore structure of PC-based materials. To address this, it is essential to examine and compare differences in the development of pore structure between AASC and PC systems, as an understanding of microstructural variations such as porosity, pore size distribution and pore tortuosity is key to optimising the durability characteristics [4, 9-11].

As a topologically complex three-phase porous medium, full description of pore structure of cementitious material over micro and macro scale remains a conundrum. While numerous studies have been carried out to assess the pore connectivity of PC systems using conventional methods such as mercury intrusion porosimetry, nitrogen gas sorption and scanning electron microscopy (SEM), these techniques cannot assess the connectivity of pores directly. This is particularly true for AASC systems, which are reported to have higher proportions of mesopores than PC systems [10-11] and poorer permeation properties for a given compressive strength grade [4, 12-13]. Therefore, accurate interpretation of these observations requires further study on pore network

connectivity (tortuosity) of AASC systems.

New technologies, e.g. μ-CT, provide us with new vision at microscopic scale of pore geometry. The micro-CT is the cross-sectional imaging of an object from either transmission or reflection data collected by illuminating the object from many different directions [9]. With this technique, it is possible to reconstruct an entire pore network ranging from micropores and macropores and three dimensional pore networks can be analysed and their topology, such as connectivity, tortuosity, and average length can be assessed. However, the transfer of μ-CT technique from the area of fundamental research to the solution of practical engineering problems is only beginning. The first ever three-dimensional pore structure characterisation of alkali-activated binders was recently carried out by Provis et al [9]. Based on X-ray micro-tomography, much lower tortuosity was reported for AASC systems compared to PC controls after 28 days, albeit that these observations did not include assessment of microstructural development during the hydration process.

In this work, the main objective has been to propose a method that is capable of investigating the pore structure development of the AASC systems. In this respect, the electrical response was analysed as a simple technique satisfying the dual requirements of physical consistency assessment and computational simplicity. It also provides additional benefits, such as a technique that can be used to monitor the performance variation of AASC on site. Therefore, the electrical pore solution conductivity and electrical resistivity of AASC and PC samples were determined and analysed using Archie's law. SEM and reconstructed X-ray microtomography techniques were applied as an aid in the interpretation of conclusions derived from electrical responses.

2. Theoretical considerations to assess pore connectivity

The analysis of pore connectivity in cementitious materials is fundamental to the general understanding of their physical properties. The estimation of tortuosity of pores in cement-based materials is not straightforward, due to multi-scale pore size distribution and complex configurations of irregular pore geometry. Whilst the complexity and characteristics of microstructure are typically captured through microscopic examinations [5, 7, 9], the sample volume analysed is so small that observations are generally not statistically representative of the holistic pore connectivity at a macroscopic scale. Therefore, a less ambiguous evaluation of pore structure is required for the method to be practical and widely applied.

Cementitious materials made of nonconductive solid phases containing electrolyte solutions may conduct electric current by the movement of free ions in the bulk solution and ions adsorbed to matrix surfaces. Several

authors [14-16] have shown that electrical conductivity of cement-based materials is a useful parameter to examine pore structure characteristics and transport properties. Such a procedure is also very attractive for in situ applications, distinct from most conventional lab-based microstructure analytical techniques [17-19]. Against this background, the theoretical basis adopted in this study was to use electrical responses to assess pore tortuosity of AASC systems, with the majority of supporting theoretical analyses derived from the field of characterising conventional PC-based systems.

The electrical conductivity of cement-based materials is a function of several factors, including the connectivity of capillary pores, level of pore saturation, and concentration and mobility of ions in the pore water as well as the geometrical configuration of electrodes used for the measurement [20-21]. Since the electrical conductivity of solid and void phases (10^{-9} and 10^{-15} S/m respectively) is several orders of magnitude lower than that of the liquid phases (1-20 S/m), the former two are generally considered as non-conductive. Therefore, an equation describing the electrical conductivity of hardened cementitious materials is [16, 20-21]:

$$C_t = C_0 \phi \beta \qquad \text{Equation (1)}$$

where C_t is the bulk conductivity of a mortar specimen (S/m), C_0 is the conductivity of pore solution (S/m), ϕ is the liquid-filled porosity (%), β is the pore connectivity factor.

Hardened PC- or AASC-based mortar consists of solid phases (sand, un-hydrated particles and hydration products), a liquid phase (pore solution) and empty pores. Hydration processes lead to an increase of the solid phase volume and subsequent alterations to the porosity, and volume and ions concentration of the liquid phase [2, 5], all of which are reflected in varying electrical responses of the systems. Experimentally, Eq. (1) can be applied to estimate the connectivity factor, provided the bulk conductivity of a mortar specimen, the conductivity of pore solution and the liquid-filled porosity are also determined.

3. Materials and methods

3.1 Raw materials

Ground granulated blast furnace slag (GGBFS) provided by Chongqing Iron and Steel Company was initially ground for 40 mins in a ball mill, after which its specific area and density were measured. The GGBFS had a Blaine fineness of 430 m^2/kg and and density of 2.80 g/cm^3. PC confirming to GB175-2007 [22] with a Blaine fineness and density of 335 m^2/kg and 3.15 g/cm^3 respectively was used to manufacture comparison specimens. **Table 1** summarises the chemical compositions of the GGBFS and PC used. The sulphite content of GGBFS

was 0.23 wt. % SO_3, which is within the limit specified in GB/T 18046-2008 (<4.0% for GGBS) and that of the PC was 2.58 wt. % SO_3, which is within the limit of 3.5% in GB/T 175-2007 [22]. It maybe noted that the clinker normally contains less than 0.5 wt. % SO_3 and most SO_3 comes from gypsum added in clinker to control the setting behaviour [22].

Activator for the AASC mixes was liquid sodium silicate with a modulus 1.2, defined as the mole ratio of SiO_2 to Na_2O, prepared by mixing NaOH solution and liquid sodium silicate in a pre-calculated ratio (12.07% Na_2O, 29.03% SiO_2 and 51.40% H_2O by mass). The activating solution was cooled in a room at a constant temperature of 20 (± 1) ^oC for 2 hours prior to mixing to avoid potential influences of dissolution heat on experimental results. A constant alkaline concentration of 5% by mass of GGBFS (Na_2O equivalent) was used in this study.

Medium graded natural sand with a fineness modulus of 2.60 was used as fine aggregate. The moisture content of sand was controlled by drying in an oven at 105 (± 5) ^oC for 24 hours, followed by cooling in a room at a temperature of 20 (± 1) ^oC and a relative humidity of 50 (± 10) % before mixing.

3.2 Samples preparation

Table 2 shows details of the mix proportions used for the AASC and PC mixes, which included four sets of both mortar and paste specimens with the same w/b. For AASC mixes, the water for the calculation of w/b refers to the sum of water from the activator and external water. The mortar specimens were formulated with a sand to binder ratio of 3:1 by mass. Mortar specimens prepared included 40 mm cubes and 40×40×160 mm prisms, whilst paste was cast in cylinder moulds with 40 mm diameter and 100 mm height. After mixing, specimens were compacted on a vibration table until no air bubbles appeared on the surface and then covered with thick polythene sheets. All specimens were de-moulded after 24 hours and subsequently cured in water at a constant temperature of 20 (±2) ^oC until testing. The 40 mm mortar cubes were used for measuring the bulk electrical conductivity. The paste specimens were used to extract pore solution for conductivity, accessible porosity and microstructural feature analysis.

3.3 Test methods

3.3.1 Flexural and compressive strength

Compressive and flexural strengths were determined according to the Chinese National Standard GB/T 17671-1999 [23] at the age of 3, 7, 14 and 28 days. All results of flexural strength and compressive strength reported are the average value of 3 and 6 specimens respectively.

3.3.2 Bulk electrical conductivity

The resistivity of mortar samples was tested using a two-point uniaxial method with an LCR bridge [24] as illustrated in **Fig. 1**. Prior to measurements, excess surface moisture was removed from the specimens and they were then placed between two thin parallel metal plates and two pieces of moist sponge, as shown in **Fig. 1**. The moisture content of the sponge pieces were controlled by dipping them fully in water to wet them completely and then applying uniform pressure to squeeze the water out. All the measurements were carried out during a period of less than 2 minutes so that any variation in moisture content of the sponge on the measurements could be minimised. Alternating current (AC) with a frequency of 1 kHz was applied in order to reduce the effect of polarisation [25] and the whole testing process lasted for less than 2 minutes. The impedance values from the measurements were converted to resistance values by the LCR bridge, from which the electrical resistivity was calculated, using the following equation:

$$\rho = \mathrm{R}\frac{\mathrm{A}}{\mathrm{l}} \qquad \text{Equation (2)}$$

where ρ is the electrical resistivity (Ω·m); R is the resistance of a uniform specimen (Ω); A is the cross-section area of a specimen (m^2); and l is the length of the specimen (m). These values were then used to calculate the conductivity (S/m) of each specimen as the inverse of the electrical resistivity.

3.4.3 Accessible porosity

The accessible porosity was assessed through measurements of capillary porosity, which is a measure of the relative volume of pores saturated with solution held by capillary forces. Based on the findings of previous research [4, 26], capillary porosity was determined based on mass differences between water-saturated and dried pastes at different temperatures. At the age of 3, 7, 14 and 28 days, paste samples were crushed to particle sizes of around 10 mm and immersed in a solution of pure ethanol to stop further hydration. Samples were then dried in a 40 ^{o}C vacuum oven and the mass recorded as $M_{40^{o}C}$ (g). The vacuum was applied in the drying process to avoid the problem of carbonation which could block the pores and affect the final results. The vacuum pressure was around 40-60mm Hg, which would not destroy hydration products, e.g. ettringite [27]. Dried samples were then immersed in deionised water for 24 hours, after which saturated surface dry mass was recorded as Ms (g). The volume of crushed samples was determined using Le Chatelier Flask's method [28]. The porosity was then computed according to the following equation:

$$\phi = \frac{\mathrm{M_s} - \mathrm{M_{40℃}}}{\rho_{\mathrm{w}}\mathrm{v}} \times 100\% \qquad \text{Equation (3)}$$

where ∅ is the paste capillary porosity (%); M_s is the mass of saturated sample (g); $M_{40℃}$ is the constant mass of

samples dried at 40 °C (g); ρ_w is the density of water (g/cm^3); and v is the bulk volume of cement paste (cm^3). The processes undertaken to determine accessible porosity are shown in **Fig. 2**.

In a mortar sample, the volume of sand was regarded as a constant value and it is known from other published research that there is no interfacial transition zone (ITZ) in AASC mortars and concretes due to the uniform distribution of hydration products throughout their structure. Therefore, based on the paste capillary porosity calculated from Equation (3) combined with the mix designs (**Table 2**), the mortar capillary porosity was derived from Equation (4):

$$\phi_m = \frac{(V_m - \frac{m_s}{\rho_s}) \times \phi}{V_m} \quad \text{Equation (4)}$$

where $\emptyset_m$ is the mortar capillary porosity (%); V_m is the volume of mortar (cm^3); m_s is the mass of sand (g); ρ_s is the density of sand (2.65 g/cm^3).

3.4.4 Analysis of pore solution

The pore solution from both AASC and PC paste samples was extracted using equipment used in conjunction with a compression machine, as shown in **Fig. 3**. One day before each test, specimens were removed from the aforementioned water curing conditions and pre-conditioned in a standard environment at 20 (±1) °C, RH ≥ 95% for 24 hours to achieve a saturated surface dry state.

The pore solution was extracted under a constant pressure of 407.6 MPa (800 kN on 1962.5 mm^2) for 45 minutes and the electrical conductivity measured immediately using a conductivity probe (Company: INESA, DDS-11a). Further details of this experimental method are described by Vollpracht et al. [29].

3.4.5 Microstructure analysis

SEM and reconstructed micro X-ray Computed Tomography (μ-CT) analysis were employed to verify the conclusions derived from interpretations of the electrical responses. Samples for SEM tests were sourced from the crushed paste specimens, which were then vacuum dried for 3 days at a constant temperature of 40 (±1) °C. Specimens were coated with gold using a sputtering device and a TESCAN VEGA 3 LMH fitted with a tungsten filament emission source was used to capture the images. Observations were undertaken at an accelerating voltage of 20 kV with a secondary electron (SE) detector [4, 30].

Micro X-ray Computed Tomography (μ-CT) is a powerful technique that can reconstruct 3D models appropriate for investigating microstructural features of cement-based materials [9, 31]. Paste samples removed from the crushed cubes with a size around 1 mm were analysed using an XRADIA MicroXCT-400 High

Resolution 3D X-ray Imaging System (ZEISS, Germany). Pores in cementitious materials often range over orders of magnitude and different pore domains, e.g. micro-pores and macro-pores, might have quite different representative elementary volumes [9,14,31]. The reconstruction of the pore system that is representative requires pore connectivity imaging using large samples at a high resolution. However, for a given μ-CT the spatial resolution is negatively correlated with the sample size; that is, it cannot be used to test relatively larger size (20mm or bigger) mortar samples. Further, even for paste samples, only a limited pore domain can be separately imaged with sufficient spatial resolution within their representative volume.. It has been reported that the hydration products of AASC are uniformly distributed and no obvious gradients are found near the interface of aggregates, e.g. interfacial transition zone (ITZ) [32, 33]. Indeed, the ITZ does show significant effects on performance of concrete, especially for transport properties [18,21,26,27], but for the purpose of this study the absence of ITZ in AASC reported by other researchers could be used to justify testing paste specimens. However, due to the limitations with the resolution of the μ-CT tomography it is better to be used for verifying the interpretations of the electrical resistivity measurements.

Measurements were carried out with hard X-ray synchrotron radiation with 0.18° per step, thereby requiring 2000 steps per rotation (360^{o}). To account for the somewhat irregular size and shape of the crushed paste samples [9], a fixed field of view with diameter 500 nm was used in the horizontal plane of detection. Each measurement gave around 1000 X-ray tomography images with a resolution of 1024×1024 pixels recorded by a Charge-coupled Device (CCD) camera. Image resolution ratio was in the order of 2 μm and images were reconstructed to a 3D model using a program written in Java.

4. Results and discussion

4.1 Mechanical properties

Mechanical properties of the AASC and PC mortar specimens at different ages are plotted in **Fig. 4**. As expected, both the compressive and flexural strengths increase with age for both materials, albeit at different rates. More specifically, AASC mortars exhibited rapid compressive strength gains during the first 14 days, yielding pronounced differences between the two binder types for both w/b. This can be attributed to faster rates of chemical reaction between alkali-activator and slag particles in AASC [34]. However, the compressive strengths of AASC mortars in this study were slightly lower than those reported by Pu et al. [35] and Fernández-Jiménez [36]. It is known that mechanical properties of AASC systems are influenced by numerous factors, including

type of slag, usage of activator (including method of addition, dosage and type) and curing conditions [37-38]. The lower strengths noted in this study are believed to be due to differences in chemical composition and fineness of the GGBFS in this study compared to that by both Pu et al. [35] and Fernández-Jiménez [36]. At the age of 28 days, the differences in compressive strength between the AASC and PC mortars were significant for 0.35 w/b mixes, whilst no obvious differences were noted for the 0.50 w/b mortars. The flexural strength results in **Fig. 4-b** show that, although AASC mortar with a w/b ratio of 0.35 out-performed the PC control, the opposite trend was noted for specimens with a w/b ratio of 0.50.

Despite limited previous research investigating the stress-strain behaviour of AASC-based materials, they are reported to exhibit brittle behaviour associated with a high prevalence of micro-cracking [34, 39]. The ratios of flexural to compressive strength at different ages for the mixes in **Fig.4-c** demonstrate a lower value for AASC mixes compared to the PC mixes, which could be due to the brittleness of AASC materials relative to the PC controls.

4.2 Bulk electrical conductivity

Electrical conductivity results for the mortar specimens are presented in **Fig. 5**. As expected, bulk electrical conductivity of both the AASC and PC mixes exhibited a decreasing trend with age, especially during the first 7 days. For the 0.35 w/b, between 3 and 28 days conductivity values decreased from 84.9 mS/m to 41.9 mS/m for the AASC mortar samples and from 58.3 mS/m to 21.8 mS/m for the equivalent PC mixes. Differences between the AASC and PC mixes were more pronounced for the 0.50 w/b mixes, with the change in conductivity values between 3 and 28 days noted as from 192.0 mS/m to 66.0 mS/m for AASC mixes and from 97.8 mS/m to 28.4 mS/m for the PC mixes. It is well established that bulk electrical conductivity of concrete is a function of solid and liquid phases, as well as voids in the matrix. Owning to ongoing hydration, solid phases and pore tortuosity increase, leading to decreases in electrical conductivity [16, 18]. Another key factor influencing conductivity of both AASC and PC mixes is w/b. More liquid is present in a given sample as its w/b ratio increases, resulting in higher conductivity. In the case of AASC mixes, however, increase in w/b decreases the concentration of alkali-ions present, provided the total alkali content is kept constant. As such, the degree of GGBFS hydration decreases with increasing liquid phases. Due to this difference from conventional PC mixes, AASC mixes are more sensitive to w/b.

The results presented in **Fig.5** are much higher than those reported in previous publications for AASC mixes, with conductivity reported to be in the range of 3.1-7.7 mS/m [18, 40]. However, these studies were

carried out using concrete rather than mortar specimens and adopted longer and different curing regimes than those used in the current study. Although these previous investigations reported AASC concretes to have lower conductivity than PC concretes in the longer term (60-90 days), no early age results were reported for comparing with the current study. Early age behaviour is clearly closely linked to ion concentration and pore connectivity, as indicated in Eq (1); both these effects will be discussed in the following sections.

4.3 Accessible porosity and pore solution conductivity

Pore connectivity was estimated for each mix using values of bulk conductivity, accessible porosity and pore solution conductivity. This section provides data for the latter two parameters. **Figure 6** presents values of accessible porosity, which for both the AASC and PC mortar mixes generally decreased with both age and w/b, as expected. Also clear from **Fig. 6** is that the PC mortar mixes were more porous than the AASC mixes. This finding agrees with the previous work [4], which from mercury intrusion porosimetry analysis showed that AASC-based materials contain fewer pores with diameters greater than 100 nm than PC materials, regardless of water to binder ratio. Similar trends are reported elsewhere in the literature [9, 12, 41-42].

The electrical conductivity of pore solutions in both AASC and PC are given in **Fig. 7**, which similarly shows decreasing trends as a function of age. In this instance, however, values for the AASC mortar mixes were higher than for the PC controls. This was particularly apparent at a w/b of 0.35, where the AASC mix exhibited markedly higher pore solution conductivity values, especially at early ages. The differences between mixes noted in **Fig. 7** are similar to those reported in previous research [18] and attributable to disparities in the hydration processes inherent to each binder type. PC reacts with water by releasing ions in the liquid phase to form hydration products including C-S-H gel, AFm, AFt and calcium hydroxide. Once hydration and precipitation are nearly completed, concentrations of ions in liquid phases remain stable. For AASC, reaction is virtually between slag particles and alkali solution and the initial ion concentration is extremely high. As GGBFS continues to hydrate in the latter case, ions in the alkali solution keep on reacting with slag particles and combine with the hydration products. The sodium silicate solution provides the essential $[SiO_4]^{2-}$ and Na^+ in C-(N)-A-S-H gel [43], then the ion concentration decreases sharply with the hydration of slag [44-45].

4.4 Pore connectivity

Pore connectivity factor (β) was calculated from the recorded values of bulk electrical conductivity, accessible porosity and pore solution electrical conductivity, using Eq (1). **Figure 8** shows the estimated connectivity factor of AASC and PC mixes at different ages, in which higher values correspond to more continuity of pores in a

sample.

The influence of w/b was apparent for the PC mortar mixes, with connectivity factor values for the 0.50 w/b mixes on average 57% higher than that for the 0.35 w/b mixes across the range of ages considered. A similar but much more pronounced effect was clear for the AASC mortar mixes. In this instance, the 0.50 w/b mix results were on average 179% higher than that corresponding to the 0.35 w/b specimens, indicating AASC's sensitivity to w/b changes. In terms of relative performance, the results highlight that equivalent performance is not achieved by AASC and PC mixes with equal w/b ratios. Indeed, in this study similar performance was achieved by the AASC mixes with a w/b of 0.35 and the PC specimens with a w/b of 0.50. Based on the findings presented in **Figs. 4** and **8**, therefore, it can be concluded that despite exhibiting equivalent or higher compressive strength than PC controls, AASC mortar mixes are likely to perform less well in terms of transport properties. In their work, Provis et al. [9] compared AASC paste with a w/b of 0.4 and PC paste with a w/b ratio of 0.5 and concluded that the tortuosity for the latter is significantly higher for a given porosity. This also agrees with previous research that reports AASC concretes to perform less well in terms of carbonation [13], water sorptivity [4, 41-42] and air permeability [4] compared to conventional PC concretes.

Whilst numerous literature sources report AASC concrete to outperform PC concrete in terms of diffusivity of chloride ions [11, 18, 46], most researchers emphasise that pore solution ion concentrations such as alkalis play an important role in this regard [11, 18, 47]. As ionic exchange between chloride and hydroxyl ions has a dominant influence on chloride ingress [18, 47], slow rates of chloride transport are observed for AASC-based materials, despite the presence of high surface chloride concentrations [18]. In order to check the conclusions drawn from pore connectivity factor data presented here, work progressed with verification experiments, including SEM observation and 3D reconstructed imaging.

4.5 X-ray computed tomography and SEM analysis

To further investigate the microstructure of the AASC and PC materials and verify the findings obtained from the electrical response-based pore connectivity results, X-ray computed tomography (μ-CT) and SEM techniques were used. Given the appropriateness of μ-CT to evaluate the 3D microstructure of porous materials [9, 19], it was used in this study to assess the extent of pore network in AASC and PC paste samples. **Figure 9** summarises the analysis procedure and results obtained from μ-CT. Two indicative μ-CT-derived slice images are given and image analysis was used to count voxel intensity and prepare histograms. Histograms of grey levels of μ-CT images typically show two sharp peaks corresponding to low density objects (pores: air and/or

water filled) and high density objects (unhydrated cement or GGBFS particles respectively) [48]. Pores were extracted from grey level images using threshold value to segment the image into two distinct populations. Such a method implies that the range of grey level within which the objects of interest appear is sufficiently narrow and homogeneous. The first step of this process involved selecting a threshold value to distinguish between void and solid (including hydration products and unhydrated particles) matrix components. Methods available for this step were to confirm and adopt a standard transition point or select a value based on structural characteristics in the raw materials [9]. With the samples studied here, a voxel intensity level of 108 was selected for the two sample types for purposes of comparison. The essential segmentation process was carried out in a Java-based programme as described in previous studies [9, 48-50].

Based on this analysis, 3D pore structure reconstructions were developed for the AASC and PC paste samples and a visual inspection of the AAS and PC specimens is shown in **Fig. 9-c** and **-g**. In cases with interconnected internal pores, the segmentation process directly separated porous and solid phases and an incompact solid skeleton was produced, from which 300 pixel cubic regions of interest (ROI) were extracted for closer analysis, as shown in **Fig. 9-d** to **-h**. The parameters for the μ-CT analysis and results of pore networks are given in **Table 3**. It is evident from results that reconstructed AASC paste solid phases are much denser than those for PC paste, as the main pore volume of PC is more than two times higher than that of AASC. This observation agrees well with results of accessible porosity (**Fig. 6**). However, the median pore volume for both AASC and PC is quite close to each other, implying the differences in pore size distribution between two binders. More precisely, the PC pore distribution is heavy trailed towards fine pores and lack of symmetry in comparison to AASC. This is clearly reflected in the high values of Kurtosis and Skewness reported in **Table 3**. Important variability can be inferred from this visual inspection. That is, the large number of separated pores in PC randomly distributes in the matrix, which could be from entrapped air, e.g. air bubbles. Meanwhile, no strong experimental evidences of highly connected pore network for AASC have been found from the segmented pores obtained form μ-CT analysis. This is an interesting pattern and it may be due to the fact that with the μ-CT test instrument used in this study, the pore structure related parameters can be imaged with the highest spatial resolution of up to 2 μm and it is not sufficient to reflect the whole range of pore structure of AASC and PC [32,35,39,40]. However, it does mean that the high pore connectivity of AASC is not due to the pores with a diameter higher than 2 μm.

Pores in AASC and PC can range over several orders of magnitude and to further investigate the connectivity, SEM was applied. **Figure 10** combines the results obtained from SEM and μ-CT analysis. Shown

in **Fig. 10-a** and **-d** are high magnification (2000×) SEM images of AASC and PC paste specimens respectively. Apparent are opposing topographies due to inherent differences between the main hydration products of the two binder systems [2, 5, 7, 9]. AASC paste hydration products have fewer topographical features and appear much denser than the PC paste hydration products. A further difference is that AASC hydration products are connected by micro-cracks, whereas isolated pores are present within PC paste samples. These features are more clearly seen at a magnification of 500, with **Fig. 9-b** and **-d**, indicating that the cracks within the AASC paste may be interconnected. Cracks in AASC-paste caused by shrinkage and low water-bonding capacity have been identified and discussed in previous related research [4-5, 10-13, 39-42] and are reported to contribute to high connectivity factors and provide potential pathways for aggressive substance permeation. Enlarged μ-CT images, **Fig. 10-c** and **-f**, also illustrate the location and variability of pores in AASC and PC. Clearly, these pores uniformly distribute in the matrix that are not connected. It would be fruitful to combine SEM and the μ-CT test in pore connectivity assessment and it can be deduced that the pores in AASC are closely connected by micro-cracks.

Based on the corroborating SEM observations and μ-CT findings generated and discussed above with the support of findings identified from the literature, it may be concluded that electrical response measurements present a viable route for monitoring pore structure changes in AASC-based materials.

5. Practical considerations

Although AASC-based materials offer an attractive alternative to conventional PC materials, numerous factors may affect its pore connectivity and, therefore, ultimate performance. It may be noted that the quality of GGBFS in most developed countries is well controlled and as a commercial product, its price sometimes could be higher than that of PC. The situation is different in countries, such as China, where the quality of GGBFS inherently fluctuates and research confirms that its chemical composition and fineness, in particular, significantly affects AASC hydration products and microstructural properties [32,34,51-54]. Equally, increasing rates of reaction between GGBFS and activators may induce more defects such as cracks due to fast setting [35, 38] and retarders may need to be applied to control this [5, 18, 35]. AASC-based materials are also more sensitive to curing [4, 12, 41] and, to achieve comparable permeation properties as that of PC materials, require longer duration in moist conditions. The pore structure of the AASC changes not only with chemical compositions of the material used and the extent of reactions, but also with changes in relative humidity, temperature and applied load.

Unfortunately, however, few systematic studies have been carried out to clarify interactions between all of these factors and it is not easy to draw a sound conclusion as to which factors play a key role in controlling AASC microstructure. Against this background, more detailed investigation needs to be carried out.

6. Conclusions

The pore structure not only influences the physical and mechanical properties of cementitious materials, but also affects environmental stability or durability. As such, the life expectancy and economics of using cementitious materials are to large extent controlled by characteristics of the pore structure, the interpretation of which can offer valuable indications of potential performance. By examining porosity, bulk electrical conductivity, pore solution conductivity and pore connectivity, as well as mechanical properties of AASC systems manufactured with the slag from China, the following conclusions have been drawn from this work:

1) For a given w/b, AASC mortar exhibits higher rates of compressive strength gain in comparison to PC at early ages, with no significant increases beyond 14 days. The flexural strength of AASC mortar is close to that of PC before 7 days, leading to low flexural to compressive strength ratios. This equates to high levels of brittleness combined with potentially high shrinkage, explaining why AASC mortar exhibits poor resistance to early age shrinkage-induced cracking.
2) Porosity results at different ages indicate that AASC mortar has generally low porosity, with no remarkable changes after 7 days for both w/b considered. For PC mortar, porosity continues to decrease up to 28 days with more significant reductions observed at the higher w/b . This indicates that AASC mortar generally has a dense microstructure.
3) The bulk electrical conductivity and the pore solution conductivity of AASC are much higher than PC before 28 days and this phenomenon was more pronounced at a w/b of 0.50. Pore connectivity factors obtained by combining findings relating to porosity indicate that AASC mortar has an interconnected pore structure.
4) SEM observations and μ-CT-derived reconstructed 3D images corroborated the pore connectivity results obtained using electrical response measurements. It was found that within 28 days, AASC materials could not achieve pore connectivity factor similar to that of PC, suggesting worse performance of AASC materials in terms of permeability and sorptivity at early ages. In order to achieve durable AASC-based pore structures, it is essential to control the ingredients and preparation processes. More importantly,

extended curing times are recommended for AASC materials.

5) The findings from the work reported here suggest that the measurement of electrical response, in conjunction with porosity and pore solution data and the application of Archie's law, offer a promising route for characterising the pore structure development of AASC materials. The approach presented may circumvent experimental difficulties of measuring pore connectivity in the field and be suitable for assessing influences of time and external factors on AASC material performance changes.

Pore structure is a complex problem influenced by many factors such as constituent material quality and preparation and curing processes. Engineering applications of AASC can only be achieved through an improved understanding of the impact of pore structure on its performance. Advances in this field will lead to AASC processing procedures yielding pore structures with high degrees of discontinuity and satisfactory levels of durability performance.

Acknowledgement

The experiments described in this paper were carried out in Chongqing University and Shenzhen University. The authors acknowledge these institutions for providing facilities and the financial support provided by National Natural Science Foundation of China (NO. 51408078), Open funds from Shenzhen University, State Key Laboratory of High Performance Civil Engineering Materials and Chongqing Jiaotong University, Venture and innovation support program for Chongqing oversea returns. Supports provided from University of Leeds, Queen's University Belfast and Ulster University during the analysis of data and preparation of this paper are highly appreciated.

References

[1] Kristensen P M. Climate Change - Global Risks, Challenges and Decisions: Synthesis Report. Eos Transactions American Geophysical Union, 2009, 93(18):182-182.

[2] Deventer J S J V, Provis J L, Duxson P. Technical and commercial progress in the adoption of geopolymer cement. Minerals Engineering, 2012, 29(3): 89-104.

[3] Meinshausen M, Meinshausen N, Hare W, Raper S, Frieler K, Knutti R, Frame D, Allen M. Greenhouse-gas emission targets for limiting global warming to 2 ^{o}C. Nature, 2009, 458(7242): 1158-1162.

[4] Yang K, Yang C, Magee B, Nanukuttan S, Ye J. Establishment of a preconditioning regime for air permeability and sorptivity of alkali-activated slag concrete. Cement and Concrete Composites, 2016, 73: 19-28.

[5] Juenger M C G, Winnefeld F, Provis J L, Ideker J H. Advances in alternative cementitious binders. Cement and Concrete Research, 2011, 41(12): 1232-1243.

[6] Turner L K, Collins F G. Carbon dioxide equivalent (CO_2-e) emissions: a comparison between geopolymer and OPC cement concrete. Construction and Building Materials, 2013, 43: 125-130.

[7] Zhang M, Yang C, Zhao M, Yang K, Shen R, Zheng Y. Immobilization potential of Cr (VI) in sodium hydroxide activated slag pastes. Journal of Hazardous Materials, 2017, 321: 281-289.
[8] PAS 8820:2016 Construction materials –Alkali-activated cementitious material and concrete – Specification[S], London, The British Standards Institution, 2016.
[9] Provis J L, Myers R J, White C E, Rose V, Deventer J S J V. X-ray microtomography shows pore structure and tortuosity in alkali-activated binders. Cement and Concrete Research, 2012, 42(6): 855-864.
[10] Collins F, Sanjayan J G. Effect of pore size distribution on drying shrinking of alkali-activated slag concrete. Cement and Concrete Research, 2000, 30(9): 1401-1406.
[11] Shi C. Strength, pore structure and permeability of alkali-activated slag mortars. Cement and Concrete Research, 1996, 26(12): 1789-1799.
[12] Collins F, Sanjayan J. Unsaturated capillary flow within alkali activated slag concrete. Journal of Materials in Civil Engineering, 2008, 20(9): 565-570.
[13] Adam A A, Molyneaux T C K, Patnaikuni I, Law D W. Strength, sorptivity and carbonation of geopolymer concrete. Challenges, Opportunities and Solutions in Structural Engineering and Construction, CRC Press, 2010: 563-568.
[14] Torquato S. Random heterogeneous materials: microstructure and macroscopic properties. Springer Science and Business Media, 2013.
[15] Snyder K A, Feng X, Keen B D, Mason T O. Estimating the electrical conductivity of cement paste pore solutions from OH^-, K^+ and Na^+ concentrations. Cement and Concrete Research, 2003, 33(6): 793-798.
[16] Rajabipour F, Weiss J. Electrical conductivity of drying cement paste. Materials and Structures, 2007, 40(10): 1143-1160.
[17] Kazakis N, Vargemezis G, Voudouris K S. Estimation of hydraulic parameters in a complex porous aquifer system using geoelectrical methods. Science of the Total Environment, 2016, 550: 742-750.
[18] Ma Q, Nanukuttan S V, Basheer P A M, Bai Y, Yang C. Chloride transport and the resulting corrosion of steel bars in alkali activated slag concretes. Materials and Structures, 2016, 49(9): 3663-3677.
[19] Hamamoto S, Dissanayaka S H, Kawamoto K, Nagata O, Komtatsu T, Moldrup P. Transport properties and pore-network structure in variably-saturated Sphagnum peat soil. European Journal of Soil Science, 2016, 67(1): 121-131.
[20] Archie G E. The electrical resistivity log as an aid in determining some reservoir characteristics. Transactions of the AIME, 1942, 146(01): 54-62.
[21] Rajabipour F. Insitu electrical sensing and material health monitoring in concrete structures. Ph.D. Dissertation, Purdue University, West Lafayette, Indiana, 2006.
[22] GB-175, Common Portland Cement, Standardization Administration of the People's Republic of China, Beijing, 2007, 16 pages.
[23] GB/T 17671-1999, Method of Testing cements-Determination of strength, The State Bureau of Quality and Technical Supervision, Beijing, 1999, 9 pages.
[24] Layssi H, Ghods P, Alizadeh A R, Salehi M. Electrical Resistivity of Concrete. Concrete International, 2015, 37(5): 41-46.
[25] Trau M, Saville D A, Aksay I A. Assembly of colloidal crystals at electrode interfaces. Langmuir, 1997, 13(24): 6375-6381.
[26] Yang K, Basheer P A M, Bai Y, Magee B J, Long A E. Development of a new in situ, test method to measure the air permeability of high performance concretes. NDT and Evaluation International, 2014, 64(2):30-40.
[27] Taylor H F. Cement chemistry. 1997: Thomas Telford.
[28] Rusin, Z, Świercz, P. Volumetric strains of cement-based mortars caused by ice formation in terms of frost

resistance diagnostics. Bulletin of the Polish Academy of Sciences Technical Sciences, 2015, 63(1):35-41.
[29] Vollpracht A, Lothenbach B, Snellings R, Haufe J. The pore solution of blended cements: a review. Materials and Structures, 2016, 49(8):3341-3367.
[30] Huang Q, Wang C, Zeng Q, Yang C, Luo C, Yang K. Deterioration of mortars exposed to sulfate attack under electrical field. Construction and Building Materials, 2016, 117:121-128.
[31] Yoshito N, Susumu K. Mathematica Programs for the Analysis of Three-Dimensional Pore Connectivity and Anisotropic Tortuosity of Porous Rocks using X-ray Computed Tomography Image Data. Journal of Nuclear Science and Technology, 2007, 44(9):1233-1247.
[32] Shi C, Krivenko P V, Roy D M. Alkali-activated cements and concretes. 2005: Taylor and Francis.
[33] Brough AR, Atkinson A. Automated identification of the aggregate-paste interfacial transition zone in mortars of silica sand with Portland or alkali-activated slag cement paste, Cement and Concrete Research, 2000, 30, 849-854.
[34] Ding Y, Dai J G, Shi C J. Mechanical properties of alkali-activated concrete: A state-of-the-art review. Construction and Building Materials, 2016, 127:68-79.
[35] Pu X X, Gan C C, Wamg S D, Yang C H. Summary reports of research on alkali-activated slag cement and concrete, Chongqing Inst. Arch. Eng. Chongqing, 1988, 10:1-6 (in Chinese).
[36] Fernández-Jiménez A, Palomo J G, Puertas F. Alkali-activated slag mortars: Mechanical strength behaviour. Cement and Concrete Research, 1999, 29(8):1313-1321.
[37] AlOtaibi, Saud. Performance of alkali-activated slag concrete. University of Sheffield Special Publication 2003, 202: 467-474.
[38] Wang S D, Scrivener K L, Pratt P L. Factors affecting the strength of alkali-activated slag. Cement and Concrete Research, 1994, 24(6):1033-1043.
[39] Collins F, Sanjayan J G. Cracking tendency of alkali-activated slag concrete subjected to restrained shrinkage. Cement and Concrete Research, 2000, 30(5):791-798.
[40] Rodríguez, Bernal, Gutiérrez M D, Puertas F. Alternative concrete based on alkali-activated slag. Materiales De Construccion, 2008, 58(291):53-67.
[41] Collins F G, Sanjayan J G. Capillary Shape: Influence on Water Transport within Unsaturated Alkali Activated Slag Concrete. Journal of Materials in Civil Engineering, 2010, 22(3):260-266.
[42] Collins F, Sanjayan J G. Microcracking and strength development of alkali activated slag concrete. Cement and Concrete Composites, 2001, 23(4-5):345-352.
[43] Myers R J, Bernal S A, Provis J L. A thermodynamic model for C-(N-)A-S-H gel: CNASH_ss. Derivation and validation. Cement and Concrete Research, 2014, 66(9):27-47.
[44] Puertas F, Fernández-Jiménez A, Blanco-Varela M T. Pore solution in alkali-activated slag cement pastes. Relation to the composition and structure of calcium silicate hydrate. Cement and Concrete Research, 2004, 34(1):139-148.
[45] Song S, Jennings H M. Pore solution chemistry of alkali-activated ground granulated blast-furnace slag 1. Cement and Concrete Research, 1999, 29(2):159-170.
[46] Ismail I, Bernal S A, Provis J L, Nicolas R S, Brice D G. Influence of fly ash on the water and chloride permeability of alkali-activated slag mortars and concretes. Construction and Building Materials, 2013, 48(11):1187-1201.
[47] Lloyd R R, Provis J L, Deventer J S J V. Pore solution composition and alkali diffusion in inorganic polymer cement. Cement and Concrete Research, 2010, 40(9):1386-1392.
[48] Gallucci E, Scrivener K, Groso A, Stampanoni M, Margaritondo G. 3D experimental investigation of the microstructure of cement pastes using synchrotron X-ray microtomography (μCT). Cement and Concrete

Research, 2007, 37(3):360-368.
[49] Leite M B, Monteiro P J M. Microstructural analysis of recycled concrete using X-ray microtomography. Cement and Concrete Research, 2016, 81:38-48.
[50] Bernardes E E, Carrasco E V M, Vasconcelos W L, Magalhães A G. X-ray microtomography (μ-CT) to analyze the pore structure of a Portland cement composite based on the selection of different regions of interest. Construction and Building Materials, 2015, 95:703-709.
[51] Ogirigbo O R, Black L. Influence of slag composition and temperature on the hydration and microstructure of slag blended cements. Construction and Building Materials, 2016, 126:496-507.
[52] Gong K, White C E. Impact of chemical variability of ground granulated blast-furnace slag on the phase formation in alkali-activated slag pastes. Cement and Concrete Research, 2016, 89:310-319.
[53] Haha M B, Lothenbach B, Saout G L, Winnefeld F. Influence of slag chemistry on the hydration of alkali-activated blast-furnace slag—Part I: Effect of MgO. Cement and Concrete Research, 2011, 41(9): 955-963.
[54] Haha M B, Lothenbach B, Saout G L, Winnefeld F. Influence of slag chemistry on the hydration of alkali-activated blast-furnace slag — Part II: Effect of Al_2O_3. Cement and Concrete Research, 2011, 42(1):74-83.

Figures and Tables

List of Tables

List of Figures

Table 1 Chemical composition of GGBFS and PC (percentage by mass)

Composition	SiO_2	Al_2O_3	Fe_2O_3	MgO	CaO	Na_2O	K_2O	SO_3	LOI
Slag	31.63	13.42	1.32	9.12	36.35	0.34	0.46	0.23	0.61
PC	21.33	5.80	2.57	2.41	60.21	0.70	0.21	2.58	3.27

Table 2 Mortar mix designs

Sample type	Binder proportion (wt. %)		Activator concentration (wt. % binder)	Water/binder ratio	Binder/sand ratio
	GGBFS	PC			
Mortar	100	-	5	0.35	1:3
	100	-	5	0.50	1:3
	-	100	-	0.35	1:3
	-	100	-	0.50	1:3

Note: The paste specimens were made with the same w/b ratio.

Table 3 Parameters for X-ray computed tomography and results of pore network

Mix	Threshold value	Edge lengths of ROI box	Mean pore volume (3D)	Median pore volume (3D)	Kurtosis	Skewness
PC	108	300 and 50 pixels	94.3492	8.8477	445.4510	13.9183
AASC	108	300 and 50 pixels	37.9753	8.8963	41.0626	4.2543

Note: Skewness is a measure of symmetry, the lack of symmetry. Kurtosis is a measure of whether the data are heavy-tailed or light-tailed relative to a normal distribution.

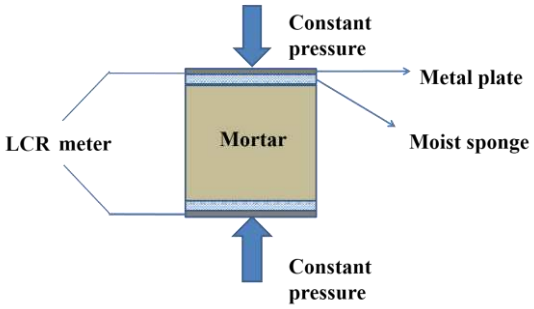

Fig. 1 Set up uniaxial method used for testing mortar resistivity

(a) Dried crushed samples (b) Immersed samples (c) Determination of volume

Fig. 2 Testing procedure of accessible porosity

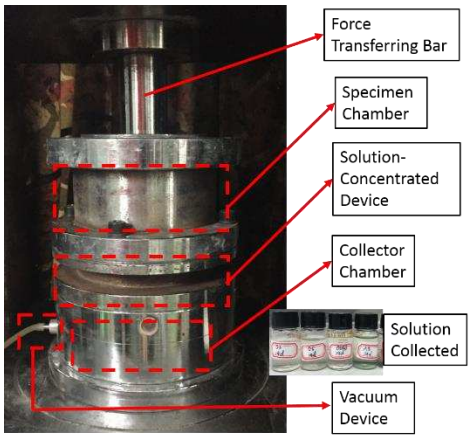

Fig. 3 High pressure pore solution extraction device (SBT, CO., LTD.)

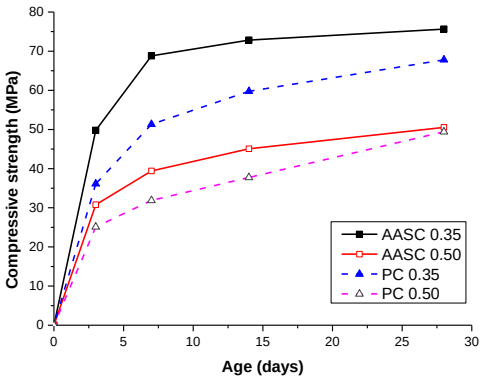

(a) Compressive strength

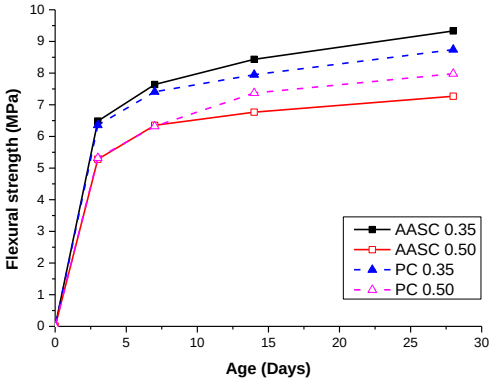

(b) Flexural strength

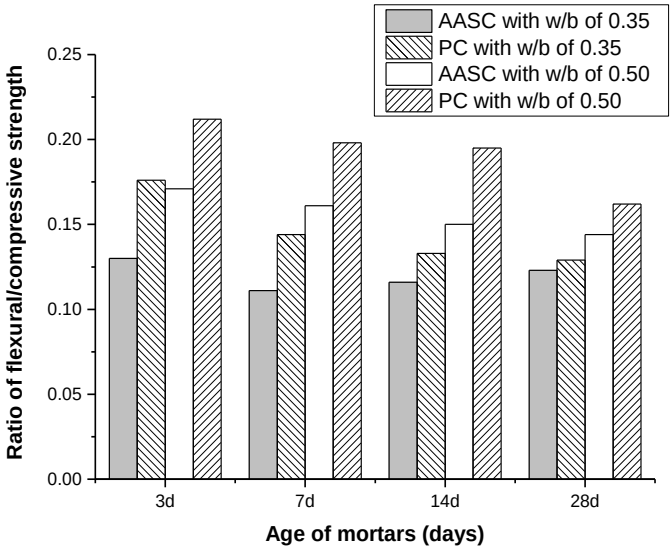

(c) Ratio of flexural/compressive strength for AASC and PC mortars

Fig. 4 Mechanical properties of AASC and PC mortars

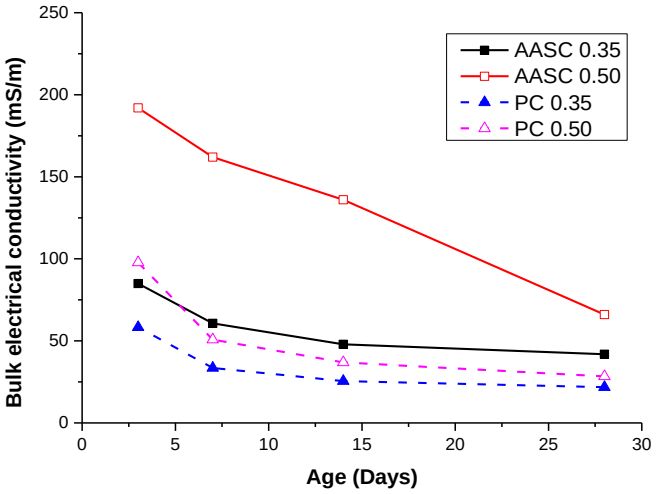

Fig. 5 Bulk electrical conductivity of mortar specimens

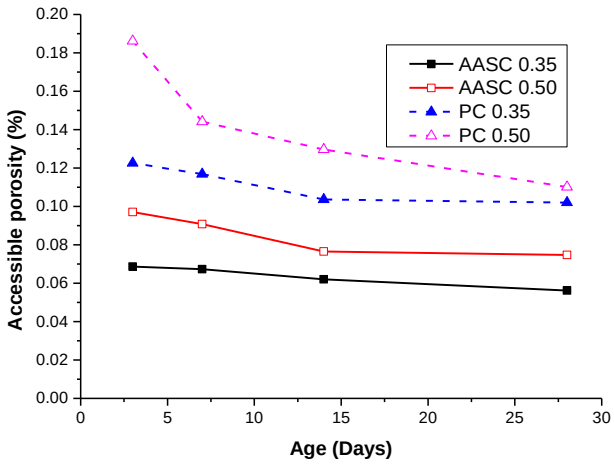

Fig. 6 Accessible porosity of mortar specimens

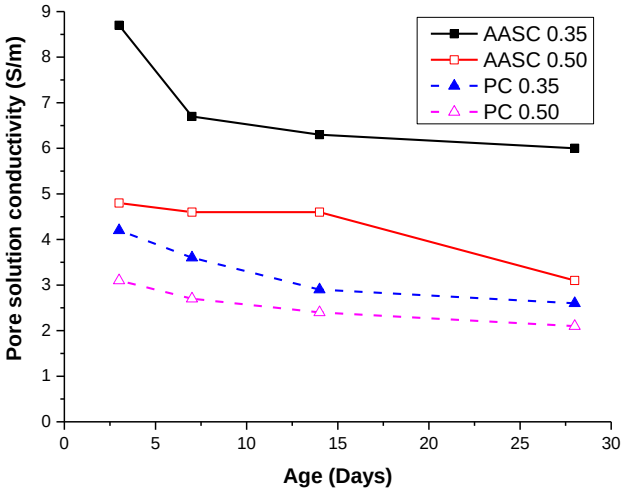

Fig. 7 Electrical conductivity of AASC and PC paste pore solutions

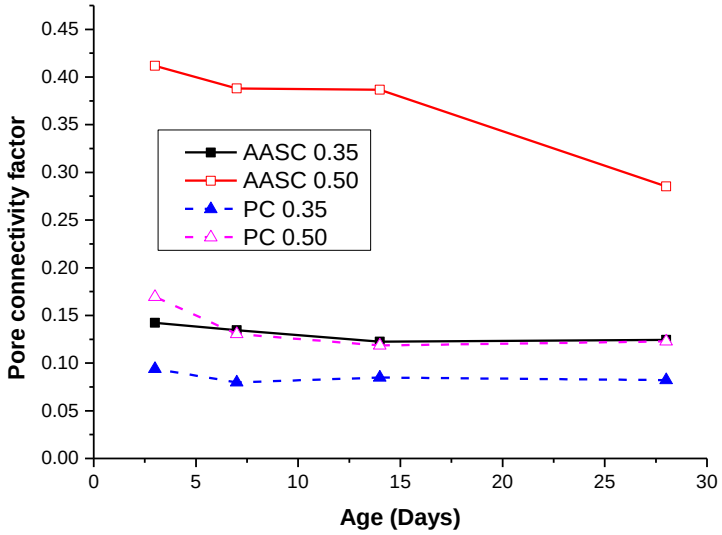

Fig. 8 Pore connectivity factors for AASC and PC mortars as a function of time

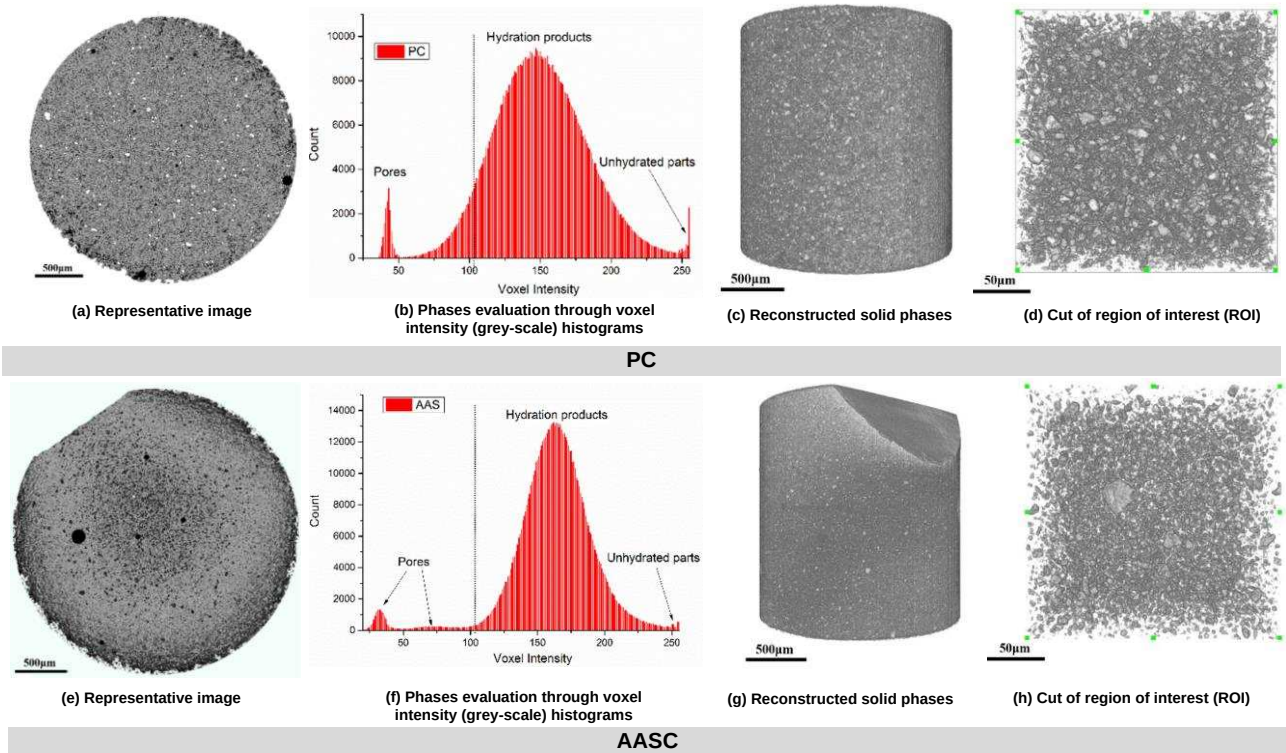

(a) Representative image | (b) Phases evaluation through voxel intensity (grey-scale) histograms | (c) Reconstructed solid phases | (d) Cut of region of interest (ROI)

PC

(e) Representative image | (f) Phases evaluation through voxel intensity (grey-scale) histograms | (g) Reconstructed solid phases | (h) Cut of region of interest (ROI)

AASC

Fig. 9 Results of reconstructed X-ray computed tomography images for PC and AASC samples

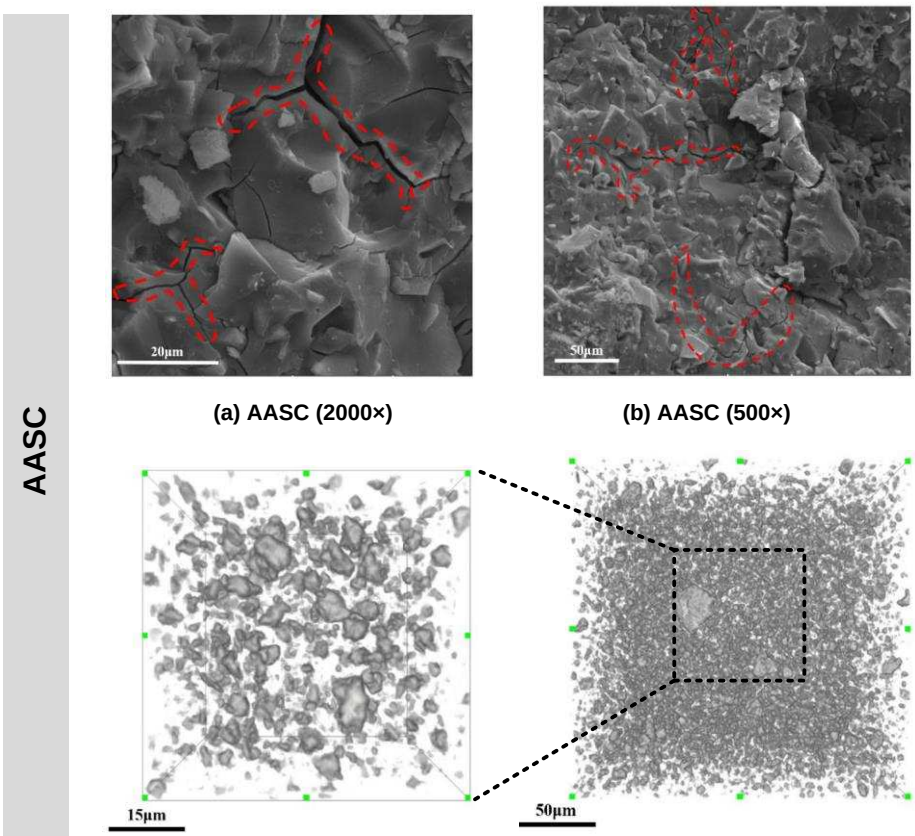

Fig. 10 SEM and μ-CT images of AASC and PC paste with water to binder ratio of 0.35 at 28 days